

Numerical simulations of bubble-induced star formation in dwarf irregular galaxies with a novel stellar feedback scheme

Daisuke Kawata,¹★ Brad K. Gibson,² David J. Barnes,¹ Robert J. J. Grand¹ and Awat Rahimi³

¹*Mullard Space Science Laboratory, University College London, Holmbury St Mary, Dorking, Surrey RH5 6NT, UK*

²*Jeremiah Horrocks Institute, University of Central Lancashire, Preston PR1 2HE, UK*

³*National Astronomical Observatory, Chinese Academy of Science, 20A Datun Road, Beijing 100012, P.R. China*

Accepted 2013 November 21. Received 2013 November 21; in original form 2013 June 26

ABSTRACT

To study the star formation and feedback mechanism, we simulate the evolution of an isolated dwarf irregular galaxy (dIrr) in a fixed dark matter halo, similar in size to Wolf–Lundmark–Melotte, using a new stellar feedback scheme. We use the new version of our original N -body/smoothed particle chemodynamics code, GCD+, which adopts improved hydrodynamics, metal diffusion between the gas particles and new modelling of star formation and stellar wind and supernovae feedback. Comparing the simulations with and without stellar feedback effects, we demonstrate that the collisions of bubbles produced by strong feedback can induce star formation in a more widely spread area. We also demonstrate that the metallicity in star-forming regions is kept low due to the mixing of the metal-rich bubbles and the metal-poor interstellar medium. Our simulations also suggest that the bubble-induced star formation leads to many counter-rotating stars. The bubble-induced star formation could be a dominant mechanism to maintain star formation in dIrrs, which is different from larger spiral galaxies where the non-axisymmetric structures, such as spiral arms, are a main driver of star formation.

Key words: hydrodynamics – ISM: bubbles – galaxies: dwarf.

1 INTRODUCTION

Dwarf irregular galaxies (dIrrs) are powerful laboratories for studying the impact of stellar feedback upon star formation and gas dynamics, because their effects are likely to be more dramatic in a low-mass system (e.g. Mac Low & Ferrara 1999). They (in this paper, we focus on a system whose stellar mass is less than $\sim 10^8 M_\odot$) are generally a gas-rich system and sustain star formation for a long time. Some of the dIrrs, e.g. Wolf–Lundmark–Melotte (WLM; Wolf 1909; Melotte 1926), are close enough for observers to resolve stellar populations in the galaxies (e.g. Minniti & Zijlstra 1997; Dolphin 2000; Rejkuba et al. 2000; Jackson et al. 2007; Bianchi et al. 2012), and detailed structures of H I gas (e.g. Huchtmeier, Seiradakis & Materne 1981; Barnes & de Blok 2004; Jackson et al. 2004; Kepley et al. 2007; Hunter et al. 2011) are observed. WLM is often considered to be the prime target for studying the intrinsic properties of star-forming low-mass systems, because it is well isolated from the rest of the galaxies in the Local Group, and it is unlikely that WLM has experienced dynamical interaction with the other galaxies in the recent past (e.g. Leaman et al. 2012). Photometric studies (e.g. Minniti & Zijlstra 1997; Rejkuba

et al. 2000; Jackson et al. 2007) reveal that WLM harbours old stellar populations. Dolphin (2000) suggested that WLM created about half of its stars in an initial strong star formation 10–12 Gyr ago. After that the galaxy maintains a low level of the star formation rate (SFR), $\sim 1\text{--}2 \times 10^{-4} M_\odot \text{ yr}^{-1}$ on average with a higher SFR in the last few Gyr. Hunter, Elmegreen & Ludka (2010) suggested a current SFR of $6 \times 10^{-3} M_\odot \text{ yr}^{-1}$ from *Galaxy Evolution Explorer* imaging data. The metallicity of stars has been measured with spectroscopic observations of individual stars and H II regions. The estimated abundances for the young supergiants show a range of $[Z]^1 \sim -0.5$ dex to -1 dex (Venn et al. 2003; Urbaneja et al. 2008), and the mean value of $[Z] = -0.87 \pm 0.06$ dex is consistent with the measured abundances for H II regions (Skillman, Terlevich & Melnick 1989; Hodge & Miller 1995; Lee, Skillman & Venn 2005). Recently, CO has been detected in WLM (Elmegreen et al. 2013). However, the CO abundance is much lower than what is expected from the current SFR and the empirical relation of the Milky Way data. The number of detailed observations are increasing recently for WLM, and even more detailed observations are being produced for other nearby dIrrs (e.g. Hunter & Elmegreen 2006; Silich et al. 2006; Hunter et al. 2010; Stilp et al. 2013). These observations

★ E-mail: dka@mssl.ucl.ac.uk

¹ $[Z] = \log(Z/Z_\odot)$.

provide strong constraints on the chemical evolution models of dwarf galaxies (e.g. Fenner et al. 2006; Gibson 2007).

Dwarf galaxies are a good target for numerical simulations which aim to model the interstellar medium (ISM), star formation and stellar feedback in a galaxy. As dwarf galaxies are physically small, the physical resolution is higher if the simulations use a similar number of resolution elements to simulations of larger galaxies, like the Milky Way. Mori et al. (1997) simulated the formation of a dwarf galaxy as a monolithic collapse of the gas within a dark matter halo. They demonstrated that due to the small gravitational potential of dwarf galaxies, the supershells created by stellar feedback owing to the star formation in the central region collide with the infalling gas and subsequently form stars, which can generate the positive colour gradient, similar to some of the observed dwarf ellipticals (e.g. Vader et al. 1988; Tortora et al. 2010). Using cosmological simulations, Ricotti & Gnedin (2005) demonstrated that the small galaxies formed at high redshifts can explain the global properties, such as the luminosity, velocity dispersion and metal abundances, of the dwarf galaxies observed in the Local Group (see also Kawata et al. 2006).

Strong feedback effects on dwarf galaxies are studied in various kinds of numerical simulations (e.g. Carraro et al. 2001; Kaufmann, Wheeler & Bullock 2007; Stinson et al. 2007, 2009; Pilkington et al. 2012; Revaz & Jablonka 2012; Bekki, Shigeyama & Tsujimoto 2013; Schroyen et al. 2013; Simpson et al. 2013; Teyssier et al. 2013), and strong feedback is considered to be a key element in building a more realistic dwarf galaxy formation model (e.g. Governato et al. 2010; Sawala et al. 2011). Carraro et al. (2001), Stinson et al. (2009) and Pilkington et al. (2011) demonstrate that because of the lower gravitational potential of dwarf galaxies, stellar feedback creates outflows of the gas and stops star formation. However, if the outflow is not strong enough to escape from the system, the gas will fall back again and restart star formation. As a result, dwarf galaxies can maintain the intermittent star formation activities, which is called ‘breathing’ star formation activity in Stinson et al. (2007). Using a monolithic collapse simulation, Kaufmann et al. (2007) and Teyssier et al. (2013) showed that strong stellar feedback makes dwarf disc galaxies thicker and puffier and leads to a more velocity-dispersion-dominated system with respect to the rotation velocity.

We have recently updated our original N -body/smoothed particle chemodynamics code, GCD+ (Kawata & Gibson 2003a; Barnes, Kawata & Wu 2012; Rahimi & Kawata 2012; Kawata et al. 2013). Kawata et al. (2013) demonstrated that the new version of GCD+ captures hydrodynamics much better than conventional smoothed particle hydrodynamics (SPH) codes used in the above-mentioned prior studies, especially for shocks induced by point-like explosions, such as a supernova (SN). We also adopt radiative cooling and heating rates, taking into account the metallicity of the gas and UV background radiation, which are ignored or simplified in some of the previous works. This improvement of the code enables us to follow smaller scale physics more accurately and justifies the use of higher resolution particles. We carry out high-resolution simulations of the evolution of a dIrr, similar in size to WLM, and study how stellar feedback affects the ISM and star formation in small galaxies. dIrr simulations with similar physical resolution were reported in Hopkins, Quataert & Murray (2011, 2012a,b), who focused on the difference between galaxies of different masses. We focus on the detailed picture of how star-forming regions affect one another, how dIrrs sustain the low level of star formation and how they maintain low metallicity. Section 2 describes briefly the new version of GCD+ and numerical models of our dIrr simulation.

Section 3 presents the results. A summary of this study is presented in Section 4.

2 METHOD AND MODELS

2.1 New version of GCD+

GCD+ is a parallel three-dimensional N -body/SPH (Lucy 1977; Gingold & Monaghan 1977) code which can be used in studies of galaxy formation and evolution in both a cosmological and isolated setting (Kawata & Gibson 2003a; Barnes et al. 2012; Kawata et al. 2013). GCD+ incorporates self-gravity, hydrodynamics, radiative cooling, star formation, SNe feedback and metal enrichment. The new version of the code includes metal diffusion patterned after the formalism described by Greif et al. (2009). We have implemented a modern scheme of SPH suggested by Rosswog & Price (2007), including their artificial viscosity switch (Morris & Monaghan 1997) and artificial thermal conductivity to resolve the Kelvin–Helmholtz instability (see also Read & Hayfield 2012; Saitoh & Makino 2013). Following Springel & Hernquist (2002), we integrate the entropy equation instead of the energy equation. As suggested by Saitoh & Makino (2009), we have added the individual time step limiter, which is crucial for correctly resolving the expansion bubbles induced by SNe feedback (see also Merlin et al. 2010; Durier & Dalla Vecchia 2012). We also implement the FAST scheme (Saitoh & Makino 2010) which allows the use of different time steps for integrating hydrodynamics and gravity. The code also includes adaptive softening for both the stars and gas (Price & Monaghan 2007), although in this current study we only implement it for the gas particles. Our recent update and performance in various test problems are presented in Barnes et al. (2012) and Kawata et al. (2013).

Radiative cooling and heating are calculated with CLOUDY (v08.00; Ferland et al. 1998) following Robertson & Kravtsov (2008). We tabulate cooling and heating rates and the mean molecular weight as a function of redshift, metallicity, density and temperature adopting the 2005 version of the Haardt & Madau (1996) UV background radiation.

We also add a thermal energy floor following Robertson & Kravtsov (2008) and Hopkins et al. (2011) to keep the Jeans mass higher than the resolution and avoid numerical instabilities (see also Bate & Burkert 1997). Following Hopkins et al. (2011), we implement the pressure floor,

$$P_{\text{Jeans}} = 1.2 N_{\text{Jeans}}^{2/3} \gamma^{-1} G h^2 \rho^2, \quad (1)$$

where $\gamma = 5/3$, and h and ρ are the smoothing length and density of the gas particle. Following Hopkins et al. (2011), we set $N_{\text{Jeans}} = 10$, and this pressure floor is adopted only in the Euler equation, i.e. the temperature of the gas is allowed to cool following the radiative cooling.

We allow the gas particle to become a star particle if the pressure of the gas particle is smaller than their P_{Jeans} and the density becomes greater than the star formation threshold density, $n_{\text{H,th}} = 1000 \text{ cm}^{-3}$ (Hopkins et al. 2013), following the Schmidt law as described in Kawata & Gibson (2003a):

$$\frac{d\rho_*}{dt} = -\frac{d\rho_g}{dt} = \frac{C_* \rho_g}{t_g}, \quad (2)$$

where C_* is a dimensionless SFR parameter and t_g is the dynamical time. We set $C_* = 1$, which is rather large, compared to $C_* \sim 0.02$ often used in these kind of simulations, including our previous work (Rahimi & Kawata 2012). However, note that the pressure of the gas particle becomes less than P_{Jeans} around $n_{\text{H}} = 10 \text{ cm}^{-3}$. This

is our resolution limit, and we set the gravitational softening limit corresponding to this density (see below). Therefore, our threshold density for star formation in this paper, $n_{\text{H,th}} = 1000 \text{ cm}^{-3}$, is much higher than our resolution limit. As a result, the gas particles experience some delay from the time they hit the resolution limit to the time when the density becomes higher than the star formation threshold. This delay is effectively similar to setting a smaller C_* value and lower star formation threshold density (see also Appendix A). We think that this is a part of the reason why high-density threshold of star formation leads to a resultant SFR independent of the parameter C_* (Saitoh et al. 2008; Hopkins et al. 2013).² We prefer $C_* = 1$ and high $n_{\text{H,th}}$ over low C_* and low $n_{\text{H,th}}$, because $C_* = 1$ allows the gas particles to turn into the star particles soon after they reach $n_{\text{H,th}}$, while low C_* allows the gas particles to survive until they reach quite high density, which slows down the simulation significantly. This choice may depend on the resolution and the kind of radiative cooling applied.

We assume that stars are distributed according to the Salpeter (1955) initial mass function (IMF). `GCD+` takes into account chemical enrichment by both Type II SNe (SNe II; Woosley & Weaver 1995) and Type Ia SNe (SNe Ia; Iwamoto et al. 1999; Kobayashi, Tsujimoto & Nomoto 2000) and mass-loss from intermediate-mass stars (van den Hoek & Groenewegen 1997), and follows the chemical enrichment history of both the stellar and gas components of the system.

2.2 Stellar feedback

The new version of `GCD+` uses a new scheme for star formation and feedback. We keep the mass of the baryon (gas and star) particles equal, unlike Kawata & Gibson (2003b) or the majority of SPH simulations which include star formation. The basic strategy for our stellar feedback was inspired by Lia, Portinari & Carraro (2002) and Martínez-Serrano et al. (2008). However, a slightly different implementation is adopted. First, every star particle formed in the simulation is randomly assigned a mass group ID ranging from 1 to 61 (although 61 is chosen arbitrarily, it is a compromised selection to sample the stellar mass range and be similar to our resolution, i.e. number of neighbour particles). Our new stellar feedback scheme models the mass, energy and metal feedback using this ID. A star cluster following the assumed IMF and the adopted remnant masses will undergo the mass-loss of about 30 per cent of their original stellar mass after the Hubble time. Therefore, star particles whose ID is between 1 and 19 are used to describe the mass-loss, energy feedback and metal enrichment. Particles with smaller IDs are responsible for feedback from higher mass stars. In our feedback scheme, 61 particles describe a whole mass range of stars in a star

² Note that the pressure floor in equation (1) enables us to ‘resolve’ the Jeans mass at a higher density than the resolution limit in our definition, i.e. where the pressure of the gas particle becomes less than P_{Jeans} , which helps to justify the high $n_{\text{H,th}}$ we adopted (Robertson & Kravtsov 2008; Schaye & Dalla Vecchia 2008). Schaye & Dalla Vecchia (2008) used a softening length much smaller than the resolution limit and let the gas clouds collapse in the dynamical time-scale till the density becomes high enough for the softening length to be effective. On the other hand, we set the softening length limit close to the resolution limit, because the smaller softening length demands smaller time steps, and it is too expensive for our high-resolution simulation. As a result, the gas collapse is slowed down, once their density reaches the resolution limit, which provides a similar effect to applying a small C_* , because our $n_{\text{H,th}}$ is higher than the resolution limit. In other words, the softening length limit is one of the parameters to control SFR.

cluster, which corresponds to $6100 M_{\odot}$ for the simulation in this paper, where the particle mass is $m_p = 100 M_{\odot}$.

Depending on their ID and age, a star particle becomes a feedback particle for some period as described below and then becomes a normal gas particle. In other words, mass-loss from stars is modelled by a star particle becoming a normal gas particle, and hence, the particle mass of gas and star particle is always equal.

The pressure from the feedback particles affects the neighbouring gas particles through the Euler equation. However, the feedback particles do not feel any reaction from the neighbour particles and follow the collisionless N -body equation for simplicity (see also Pelupessy, van der Werf & Icke 2004). The thermal energy of the feedback particles is calculated with the SPH scheme with radiative cooling and additional heating from stellar wind, SNe II and SNe Ia. Eight out of the 19 feedback particles spend no time being stars and immediately become SNe II feedback particles (Section 2.2.1), which are responsible to describe stellar feedback due to stellar wind and SNe II, and no radiative cooling is applied until their age becomes older than the lifetime of $8 M_{\odot}$ or their cooling time becomes longer than the dynamical time.

The metals produced by SNe II, SNe Ia and intermediate-mass stars are also distributed from the feedback particles to neighbouring gas particles through the metal diffusion scheme of Greif et al. (2009), i.e. the metal diffusion applied to the feedback particles is the same as the other normal gas particles. Once the age of the feedback particles becomes old enough, the feedback particle becomes a normal gas particle. Because gas density, temperature and metal abundances for feedback particles are calculated through the SPH scheme, including metal diffusion, the new gas particles inherit these properties from the feedback particles.

2.2.1 SNe II particles

We can calculate that about 13 per cent of the mass is ejected by SNe II from a star cluster following the assumed IMF and the remnant masses shown in Woosley & Weaver (1995). Therefore, each star particle in the ID range between 1 and 8 is set to be a feedback particle, ‘SNe II particle’. SNe II particles are responsible for the energy and metals produced by stellar winds and SNe II. SNe II particles are treated as one kind of particle. In other words, there is no difference between star particles whose ID is less than or equal to 8.

A star particle whose ID is between 1 and 8 becomes an SNe II particle at the same time step at which they form. This allows all the SNe II particles to be effective immediately and to maintain their effect for a long time. For example, SNe II particles with solar metallicity are responsible for mass-loss and feedback from 100 to $7 M_{\odot}$ stars. Once the age of the SNe II particle becomes older than the lifetime of $7 M_{\odot}$ star, the SNe II particle becomes a gas particle.

We assume that each SN produces thermal energy E_{SN} (erg). We also assume that stellar wind from each massive star ($>15 M_{\odot}$) produces thermal energy L_{SW} (erg s^{-1})³ and adds this to the SNe II

³ Feedback due to massive stars is often divided to several mechanisms, such as radiation pressure, photoionization heating and stellar wind (e.g. Hopkins et al. 2012a). However, we avoid introducing more complicated subgrid models or justifications, because subgrid models are often implementation dependent and associated with more parameters which affect the system in complex ways. Rather, we simply call the overall feedback effects (in our resolution and implementation) from massive stars ‘stellar wind’ and use the parameter, L_{SW} , to control energy feedback before SNe II kick in.

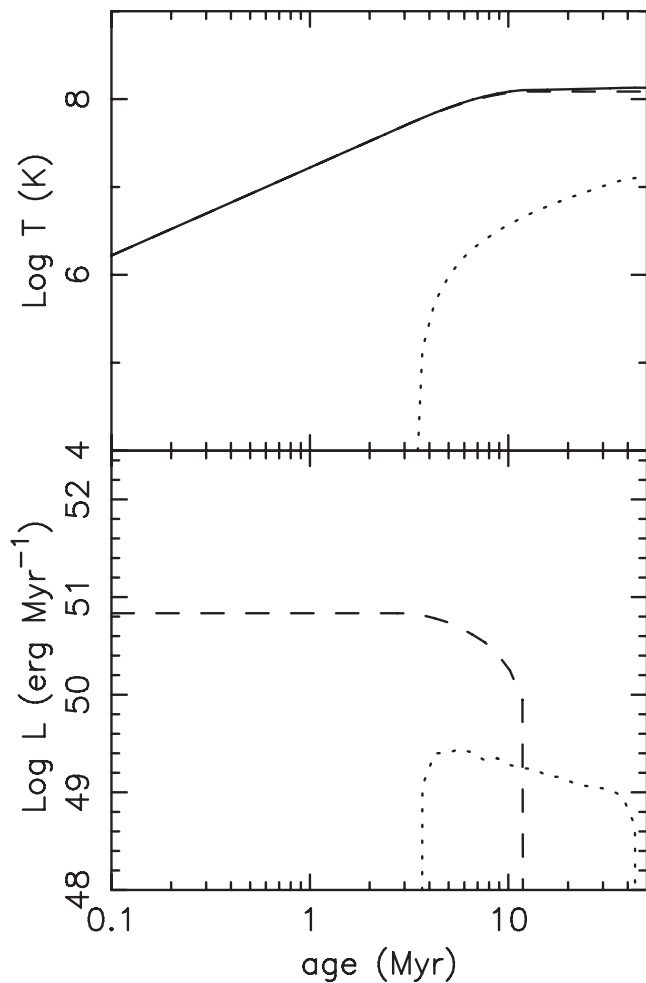


Figure 1. Upper panel: temperature evolution due to stellar energy feedback of SNe II particle with solar metallicity as a function of the age (solid line). The contribution from stellar wind and SNe II are also shown with dashed and dotted lines, respectively. Lower panel: the energy deposition rate (erg Myr^{-1}) from stellar wind (dashed line) and SNe II (dotted line) to a SNe II particle of $100 M_{\odot}$ as a function of the age. Stellar wind energy of $L_{\text{SW}} = 10^{37} \text{ erg s}^{-1}$ per massive star ($>15 M_{\odot}$) and SNe II energy of $E_{\text{SN}} = 10^{50} \text{ erg}$ per SN are assumed like our fiducial model.

particles. Because there are eight SNe II particles out of 61 star particles, each SNe II particle receives 1/8 of the energy and metals produced by a star cluster of 61 star particles, depending on the age and initial metallicity. Consequently, SNe II particles have higher temperature and become metal rich. Fig. 1 shows the evolution of temperature and the energy deposition rate of an SNe II particle with solar metallicity as a function of the age, assuming $L_{\text{SW}} = 10^{37} \text{ erg s}^{-1}$ per massive star (e.g. Weaver et al. 1977; Shull 1980; Gibson 1994; Oey & Massey 1994) and $E_{\text{SN}} = 10^{50} \text{ erg}$ per SN (e.g. Thornton et al. 1998) which are used in our fiducial model.

The pressure from SNe II particles affects the neighbour particles through the Euler equation, while SNe II particles follow the collisionless N -body equation. We calculate thermal energy for the SNe II particles following the SPH scheme, and radiative cooling is turned off. Therefore, although the temperature of the SNe II particle can increase, e.g. following Fig. 1, SNe II particles are subject to adiabatic expansion and compression, and their temperature evolution does not follow Fig. 1 completely.

We turned off radiative cooling until their age becomes older than the lifetime of $8 M_{\odot}$ or their cooling time becomes longer than dynamical time. This is similar in spirit to the blastwave feedback (Mori, Yoshii & Nomoto 1999; Thacker & Couchman 2000; Brook et al. 2004; Stinson et al. 2006). Note that we do not adopt the kinetic feedback scheme (e.g. Navarro & White 1993; Kawata & Gibson 2003a; Springel & Hernquist 2003).

We do not distribute the feedback energy to the neighbour particles, only the SNe II particle itself receives the thermal energy produced by SNe II and stellar winds. This guarantees that the SNe II particles are hot enough not to suffer from rapid cooling that is expected in a dense region such as those where stars form (Kay et al. 2002; Booth, Theuns & Okamoto 2007; Dalla Vecchia & Schaye 2012). This also means that we need to resolve the expansion of the bubble from a single SNe II particle, which requires careful choice of the numerical recipe of SPH. We have demonstrated that the new version of GCD+ is capable of resolving the expansion of a feedback bubble (Kawata et al. 2013). Consequently, our typical minimum time step is $\Delta t = 100\text{--}1000 \text{ yr}$, similar to what is used in Saitoh et al. (2008) and Hopkins et al. (2012a).

2.2.2 Other feedback particles

We apply a similar algorithm to star particles with different IDs. The IMF dictates that about 30 per cent of the mass will be ejected after a cosmic time. Therefore, star particles with IDs ranging from 9 to 19 turn back into gas particles as a function of their age, which models the mass-loss from intermediate-mass stars and SNe Ia feedback.

For example, ID 9 particles with solar metallicity represent mass-loss from 7 to $5.6 M_{\odot}$ stars. When the age of the particle becomes older than the lifetime of a $7 M_{\odot}$ star, it becomes a feedback particle. The particle inherits the original metal abundance and receives additional metals that stars in this mass range produce (van den Hoek & Groenewegen 1997), which are then diffused via the metal diffusion scheme applied. Their thermal energy is calculated with the SPH scheme, and the additional pressure from these feedback particles is applied to their neighbour particles. For these particles, we turn on radiative cooling during their mass-loss. Once the particle becomes older than the lifetime of a $5.6 M_{\odot}$ star, the particle becomes a normal gas particle.

The same algorithm is applied to the particles whose IDs are between 10 and 19, but they are responsible for different mass ranges of stars. The particles whose ID is high enough to cover the mass range of SNe Ia progenitors receive the energy from SNe Ia depending on their age. Unlike the SNe II particles, the feedback particles that received SNe Ia are allowed to be affected by radiative cooling. Because of this algorithm, the particle masses of stars and gas are always constant, and the mass resolution is kept constant.

The main free parameters of the new version of GCD+ include energy per SN, E_{SN} , and stellar wind energy per massive star, L_{SW} . These parameters control the effect of feedback on star formation, which is the most unknown and possibly most important process in galaxy formation and evolution. In this paper, we present the results of two models with and without the stellar energy feedback and explore the effect of feedback on the star formation in dIrrs. Our fiducial model, Model FB, adopts $E_{\text{SN}} = 10^{50} \text{ erg}$ (e.g. Thornton et al. 1998)⁴ and $L_{\text{SW}} = 10^{37} \text{ erg s}^{-1}$ (e.g. Weaver et al. 1977;

⁴ Various previous studies applied different values of SN energy. However, we think that the effect of feedback depends more on the implementation. Therefore, we think that this value is simply a free parameter which highly depends on the implementation.

Shull 1980; Gibson 1994; Oey & Massey 1994). We also present the results of Model noFB, where $E_{\text{SN}} = L_{\text{SW}} = 0$ are adopted. Although we turn off energy feedback in Model noFB, mass-loss and metal enrichment are included, and we also track the chemical evolution in this model.

2.3 Dwarf irregular simulations

We are interested in investigating the evolution of a dwarf disc galaxy similar in size to dIrr, WLM. We therefore set up an isolated disc galaxy which consists of gas and stellar discs, with no bulge component, in a static dark matter halo potential (Grand, Kawata & Cropper 2012; Rahimi & Kawata 2012). In this paper, we focus on the effect of feedback on the ISM and star formation in dIrrs. To highlight the evolution of baryonic components and save computational costs, we have fixed the dark matter halo potential. The shape of the dark matter halo could be altered by the evolution of the baryons in small systems like dIrrs, especially if repeated outflows occur owing to strong stellar feedback (e.g. Navarro, Eke & Frenk 1996; Read & Gilmore 2005; Mashchenko, Couchman & Wadsley 2006; Governato et al. 2010; Pontzen & Governato 2012; Di Cintio et al. 2013; Teyssier et al. 2013). However, a live halo component will complicate the evolution of the baryonic disc with effects such as numerical scattering and heating, and may even act as large perturbing masses that artificially disturb the baryonic components if the mass resolution for the dark matter is too low (e.g. D’Onghia, Vogelsberger & Hernquist 2013). It requires a careful setup and excessive computational resources. Therefore, we have elected to model the dark matter halo with static potential. We use the standard Navarro–Frenk–White (NFW) dark matter halo density profile (Navarro, Frenk & White 1997), assuming a Λ -dominated cold dark matter cosmological model with cosmological parameters of $\Omega_0 = 0.266 = 1 - \Omega_\Lambda$, $\Omega_b = 0.044$ and $H_0 = 71 \text{ km s}^{-1} \text{ Mpc}^{-1}$:

$$\rho_{\text{dm}} = \frac{3H_0^2}{8\pi G} \frac{\Omega_0 - \Omega_b}{\Omega_0} \frac{\rho_c}{cx(1+cx)^2}, \quad (3)$$

where

$$c = \frac{r_{200}}{r_s}, \quad x = \frac{r}{r_{200}} \quad (4)$$

and

$$r_{200} = 1.63 \times 10^{-2} \left(\frac{M_{200}}{h^{-1} M_\odot} \right)^{1/3} h^{-1} \text{ kpc}, \quad (5)$$

where ρ_c is the characteristic density of the profile, r is the distance from the centre of the halo and r_s is the scale radius. The total halo mass is set to be $M_{200} = 2.0 \times 10^{10} M_\odot$ and the concentration parameter is set at $c = 12$. The halo mass is roughly consistent with the recent measured mass of WLM by Leaman et al. (2012). However, it is difficult to measure the total mass up to the virial radius, and the total halo mass of the dIrr is not well constrained.

The stellar disc is assumed to follow an exponential surface density profile:

$$\rho_{\text{d},*} = \frac{M_{\text{d},*}}{4\pi z_{\text{d},*} R_{\text{d},*}^2} \text{sech}^2 \left(\frac{z}{z_{\text{d},*}} \right) \exp \left(-\frac{R}{R_{\text{d},*}} \right), \quad (6)$$

where $M_{\text{d},*}$ is the stellar disc mass, $R_{\text{d},*}$ is the scalelength and $z_{\text{d},*}$ is the scaleheight. Following the observational estimates of WLM (Jackson et al. 2007; Képley et al. 2007; Leaman et al. 2012), we adopt $M_{\text{d},*} = 1.5 \times 10^7 M_\odot$, $R_{\text{d},*} = 1.0 \text{ kpc}$ and $z_{\text{d},*} = 0.7 \text{ kpc}$.

The gaseous disc is set up following the method described in Springel, Di Matteo & Hernquist (2005). The radial surface density profile is assumed to follow an exponential law like the stellar disc

with a scalelength, $R_{\text{d,gas}} = 1.5 \text{ kpc}$. The initial vertical distribution of the gas is iteratively calculated to reach hydrostatic equilibrium assuming the equation of state calculated from our assumed cooling and heating function. The total gas mass is $3.0 \times 10^8 M_\odot$. This is significantly higher than the estimated H I gas mass in WLM (Képley et al. 2007). However, it is not straightforward to compare the total gas mass in the simulations with the H I gas mass in observations, because the gas only in the central region can be of high enough density to be identified as H I gas, due to UV background radiation. For example, although we have initially set up an exponential profile of the gas disc, the significant amount of the gas in the outer region is quickly evaporated by UV background radiation (Efstathiou 1992; Schaye 2004).

We impose initial radial abundance profiles to both gas and stellar components. The iron abundance profiles for the gas and stars are given by

$$[\text{Fe}/\text{H}](R) = -1.24 - 0.04 \frac{R}{1 \text{ (kpc)}}. \quad (7)$$

Leaman et al. (2013) measured the mean metallicity of $[\text{Fe}/\text{H}] = -1.28 \pm 0.02$ and the metallicity gradient $d[\text{Fe}/\text{H}]/d(r/r_c) = -0.04 \pm 0.04 \text{ dex}$ for WLM. The core radius of WLM is $r_c \sim 0.5 \text{ kpc}$ (Mateo 1998). Our assumed metallicity gradient is within the error of their measurement. We also add a Gaussian scatter with a dispersion of 0.03 and 0.3 dex for gas and stars, respectively, to the relation of equation (7). The α -element abundance is then determined by $[\alpha/\text{Fe}] = 0.2$ (Colucci & Bernstein 2011) with a Gaussian scatter with a dispersion of 0.02 dex. For the initial star particles, we randomly assign them an age, assuming the age–metallicity relation $[\text{Fe}/\text{H}] = -0.01 \times \text{age}(\text{Gyr})$ and a constant SFR for 10 Gyr.

We use 3000 000 gas particles and 150 000 star particles for the initial condition. This leads to $100 M_\odot$ for each particle and means that both the star and gas particles have the same mass resolution in our simulations. This is not by chance but required from our new modelling of star formation, feedback and metal diffusion shown in Section 2.1. We apply the spline softening and variable softening length suggested by Price & Monaghan (2007) for SPH particles. We set the minimum softening length at 16 pc (the equivalent Plummer softening length is about 5 pc), which corresponds to the required softening for gas to resolve $n_{\text{H}} = 10 \text{ cm}^{-3}$ with solar metallicity. Fig. 2 shows thermal pressure and gas density for gas particles at $t = 1.5 \text{ Gyr}$ for Model noFB. The grey line in the figure indicates the adopted pressure floor of equation (1). The figure demonstrates that the pressure of some gas particles at $n_{\text{H}} > 10 \text{ cm}^{-3}$ becomes lower than the pressure floor, i.e. they hit the resolution limit. We therefore used the above softening limit. For the star particles, we applied a fixed spline softening of 16 pc softening length. We run simulations for 1.5 Gyr from the initial conditions described above for Models FB and noFB (Section 2.2.2). We do not include any continuous inflow of the gas for simplicity of numerical setup. Therefore, we do not think that our simulations are capable of studying a long time evolution, which is a reason for stopping the simulation at this short period. This also helps to reduce the total computational cost. Note that in this paper, we demonstrate a dramatic evolution even in this short period. We think that our idealized numerical setup and the short period of evolution for this simulation are a compromised choice and valid for the purpose of this paper.

3 RESULTS

Fig. 3 shows the history of SFR for Models FB and noFB. The initial gas disc is smooth, and no gas particle has a high enough density

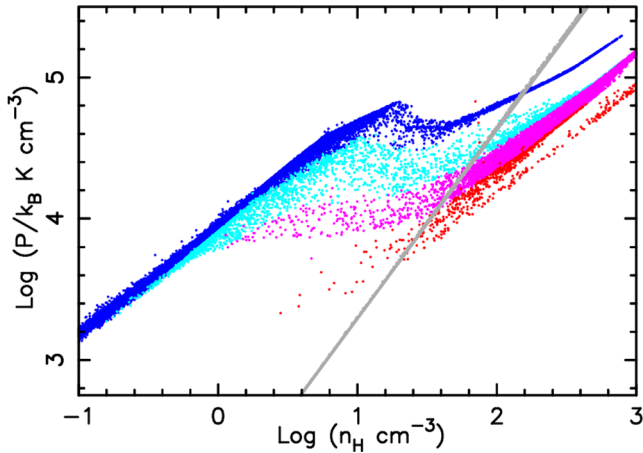


Figure 2. Thermal pressure, P/k_B , versus hydrogen number density, n_H , for gas particles with $[Z] < -0.75$ (blue dots), $-0.75 < [Z] < -0.5$ (cyan dots), $-0.5 < [Z] < -0.25$ (magenta dots) and $[Z] > -0.25$ (red dots) in Model noFB at $t = 1.5$ Gyr, where k_B is the Boltzmann constant. The grey line indicates the adopted pressure floor in equation (1).

to form stars. The gas density gradually increases especially at the centre. At around $t = 0.5$ Gyr, star formation starts happening. Fig. 3 clearly shows that the star formation history is quite different between Models FB and noFB. Model FB has stochastic star formation. This is because the gas is blown out, as shown later. The mean SFR from 0.5 to 1.5 Gyr is about $5 \times 10^{-3} M_\odot \text{ yr}^{-1}$ for Model FB, which is higher than the estimated mean SFR of WLM, about $2 \times 10^{-4} M_\odot \text{ yr}^{-1}$ (Dolphin 2000), although it is comparable to the current SFR of $6 \times 10^{-3} M_\odot \text{ yr}^{-1}$ (Hunter et al. 2010). Note that this is a significantly lower SFR than the recent simulations, including Hopkins et al. (2012a) and Teyssier et al. (2013). It could be possible to tune our star formation and feedback parameters to lower the SFR to match the observed mean SFR of WLM. However, the star formation history also depends on the initial condition, and it is difficult to explore the best parameter set from the idealized simulation. It is not our aim to fine-tune the parameters and initial condition for WLM. Rather, we compare two models with and without feedback in identical conditions and discuss the effect of the feedback on the star formation and the evolution of the ISM. Therefore, our Model FB does not mean our best model. Model FB might be an exaggerated model of feedback effect due to the high SFR,

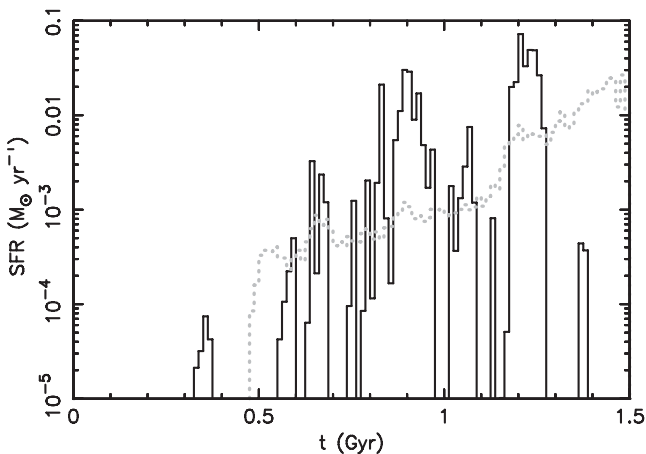


Figure 3. History of SFR of Models FB (black solid) and noFB (grey dotted).

which makes our comparison easier as a numerical experimental study.

Model noFB, on the other hand, shows a continuous increase of the SFR. Although at $t = 1.5$ Gyr the SFR reaches more than $0.01 M_\odot \text{ yr}^{-1}$, it is worth noting that in the earlier phase of the star formation (around $t \sim 0.5$ – 1 Gyr) the SFR in Model noFB is sometimes lower than that of Model FB and the mean SFR of Model noFB from 0.5 to 1.5 Gyr is about $4 \times 10^{-3} M_\odot$ which is slightly lower than that of Model FB. Because of the shallow gravitational potential and inefficient radiative cooling, it takes a long time for enough gas to fall into the central region to maintain the high SFR, if there is no perturbation in the ISM, and the gas smoothly accretes into the central region, like Model noFB. On the other hand, as we demonstrate below, in Model FB, once the star formation begins in the central region, strong feedback produces significant perturbations in the ISM and induces star formation, ‘the bubble-induced star formation’. Note that although the strong stellar feedback can enhance the star formation, i.e. positive feedback (e.g. Dale et al. 2005), for a longer time-scale, the overall effect of the stellar feedback reduces the SFR (e.g. Dale, Ercolano & Bonnell 2013).

Figs 4 and 5 show snapshots of Model FB from $t = 1$ to 1.5 Gyr. After the major burst around $t = 0.85$ Gyr, the star formation temporarily completely stops. Fig. 4 shows a hole in the gas whose radius is around 1 kpc at $t = 1$ Gyr, which causes the cessation of the star formation. Then, the gas starts reaccreting. Thanks to the inhomogeneous distribution of the gas created by the past generations of the stellar feedback, even during this accretion, the gas collapses locally often in filamentary structures and forms stars, which corresponds to a low level of SFR in $t = 1$ – 1.1 Gyr in Fig. 3. Then, once the gas falls into the central region, and the gas density becomes high enough, the concentrated star-forming region develops around the centre and causes massive stellar feedback, which creates bubbles as seen in the snapshot of $t = 1.195$ Gyr in Fig. 5. The expanding bubble collides with the accreting gas. The high-density gas owing to this collision induces the next generation of the star formation. Then, this new generation of star-forming regions creates the new bubbles in the shell of the original bubbles, which, for example, is seen around $(x, y) = (-0.5, 0.5)$ kpc in the snapshot of the face-on view of the gas at $t = 1.205$ Gyr in Fig. 5. These generations of bubbles and star formation induced by the bubbles propagate outwards and create a big hole in the gas. This eventually stops star formation again around $t = 1.28$ Gyr. Then, the expansion of the bubble stops around $t = 1.3$ Gyr and reaches a radius of more than 2 kpc. Then, the gas reaccretes again, and at $t = 1.5$ Gyr, it is still in the phase of reaccretion of the gas. This repeated star formation and the cessation due to the strong effect of the stellar feedback is called ‘breathing’ star formation activity in Stinson et al. (2007) and is demonstrated in the previous simulations (e.g. Carraro et al. 2001; Stinson et al. 2007; Teyssier et al. 2013).

Our higher resolution simulation enables us to study the bubble-induced star formation in more detail. Fig. 6 provides a close-up view of the propagation of the star formation owing to the successive generations of the bubbles created by stellar feedback. At $t = 1.185$ Gyr, star formation starts at the centre. At this time, there is a plenty of the accreted gas in the central region. Bubbles created by the first generation of star formation collide with the gas in the central region and create the high-density gas, which leads to the star formation seen in the snapshot at $t = 1.19$ Gyr. These new born stars also create bubbles and push the existing bubbles outwards. Fig. 6 shows that more gas accretes from the upper-left region of these face-on view images. As a result, more star formation

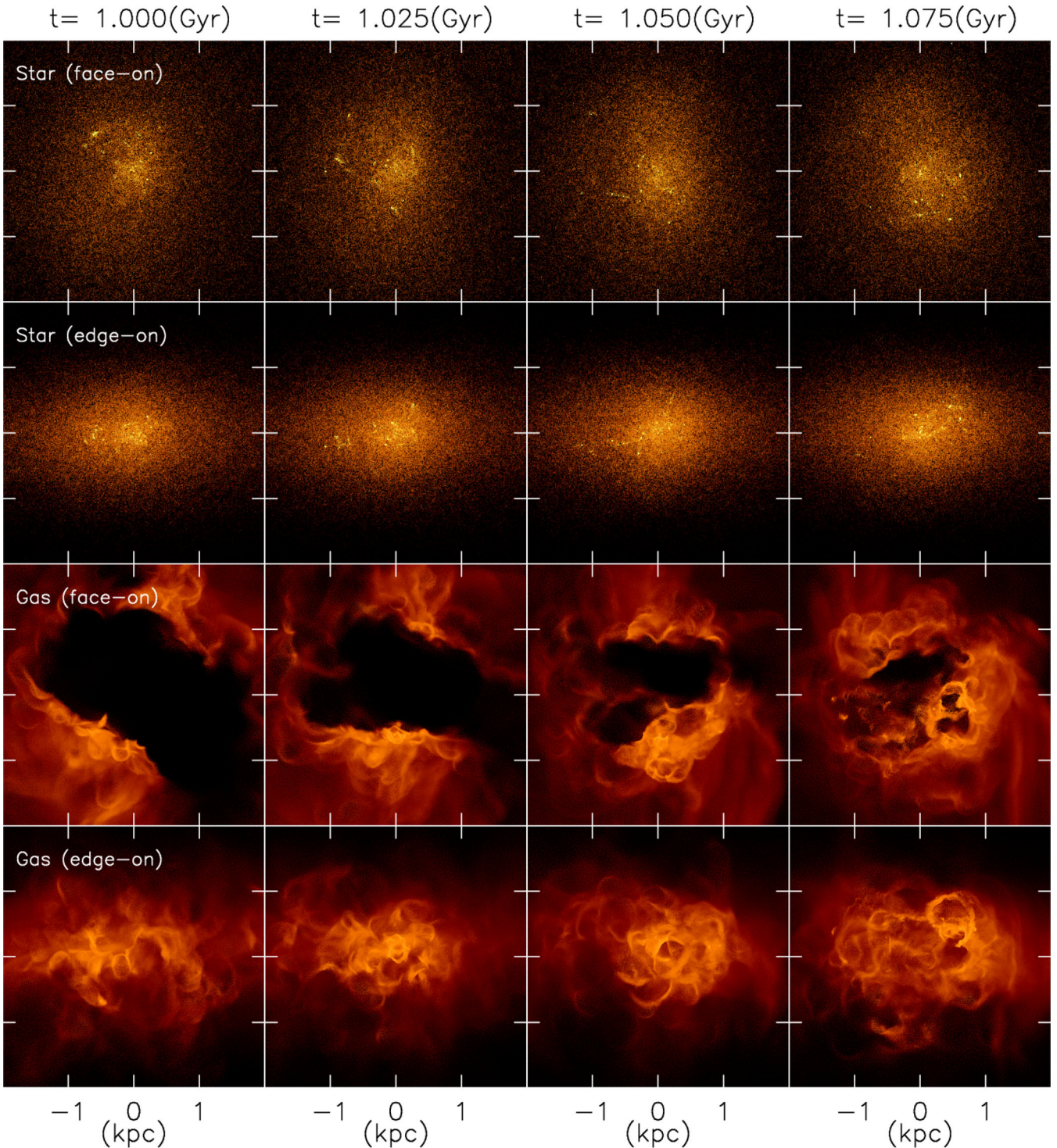


Figure 4. Snapshots of Model FB from $t = 1.0$ and 1.075 Gyr.

occurs in that region at $t = 1.2$ Gyr. A bubble with a radius of about 200 pc seen around $(x, y) = (-0.5, 0.5)$ kpc at $t = 1.205$ Gyr was likely created by the young stars highlighted at the $t = 1.2$ Gyr snapshot. We can also see from these snapshots that star formation occurs where the smaller bubbles collide with each other, which creates the high-density wall of gas. These snapshots clearly indicate that the successive star formation induced by the collision between the bubbles and/or between the bubbles and the accret-

ing gas are responsible for the continuous expansion of the largest bubble.

As a comparison, Fig. 7 shows a snapshot of Model noFB at $t = 1.5$ Gyr. The figure demonstrates that in this model the gas density can become high enough for star formation only in the central region, and stars are forming only in the central ~ 400 pc. This is because the gravitational potential is not deep enough to form the large dense disc owing to inefficient radiative

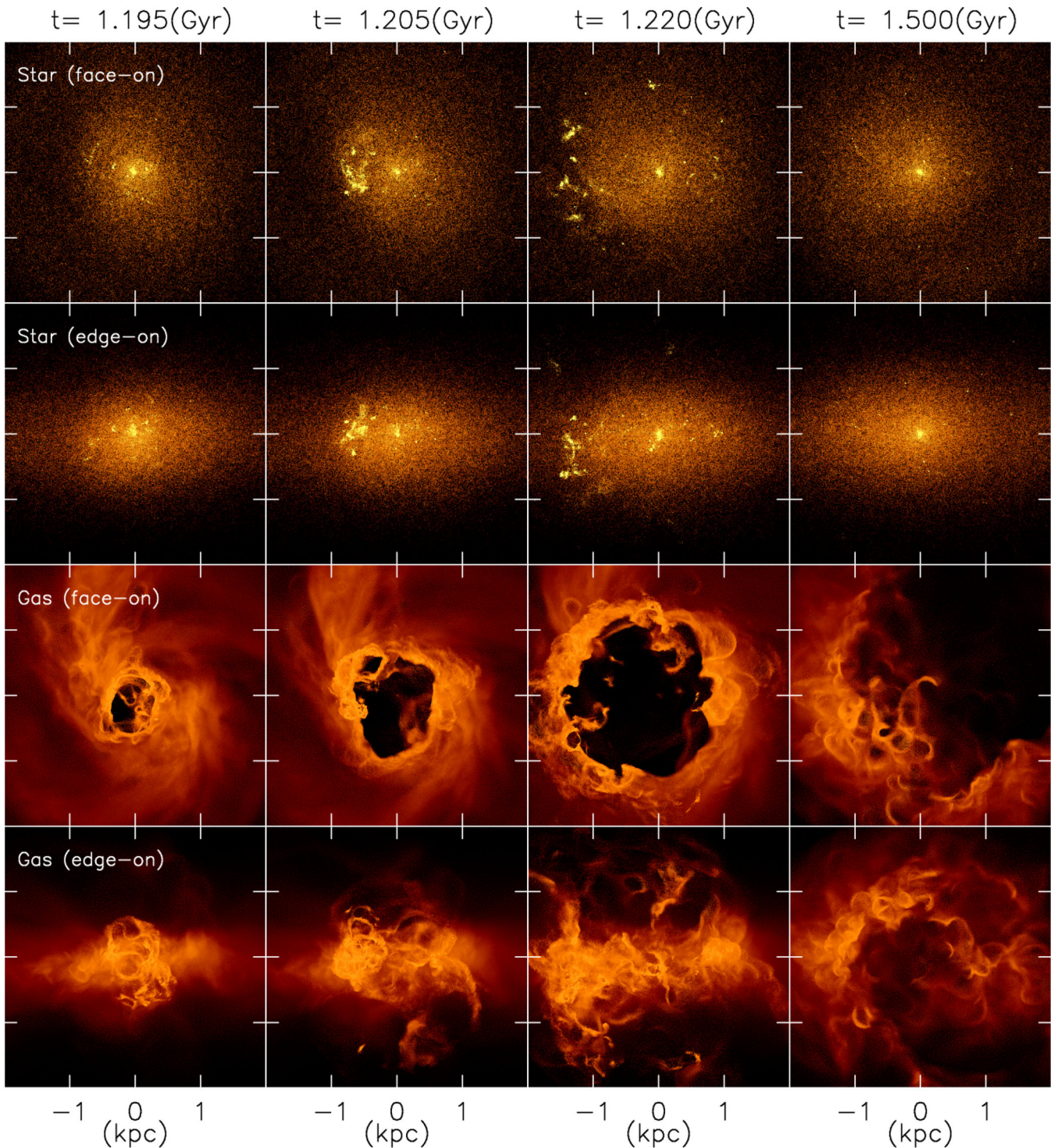


Figure 5. Same as Fig. 4, but for the outburst around $t = 1.2$ Gyr.

cooling. Therefore, the galaxy cannot develop the high-density structures, like spiral arms. The face-on view of the gas distribution in Fig. 7 displays spiral-like structure. However, they cannot become dense enough, because of shallow gravitational potential and inefficient cooling. Comparison between Models FB and noFB demonstrates that the bubble-induced star formation in Model FB ensures that the star formation spreads widely in the galaxy.

Our results infer that there could be a critical total mass or baryonic mass of the galaxy which separates the galaxies in which the bubble-induced star formation is dominant from the galaxies which harbour a gas disc with high enough density to develop local instabilities and non-axisymmetric structures, such as spiral arms, that may trigger star formation. Unfortunately, using our idealized simulations, we cannot explore the critical mass which must be sensitive to many different factors, such as the shape of dark matter halo and

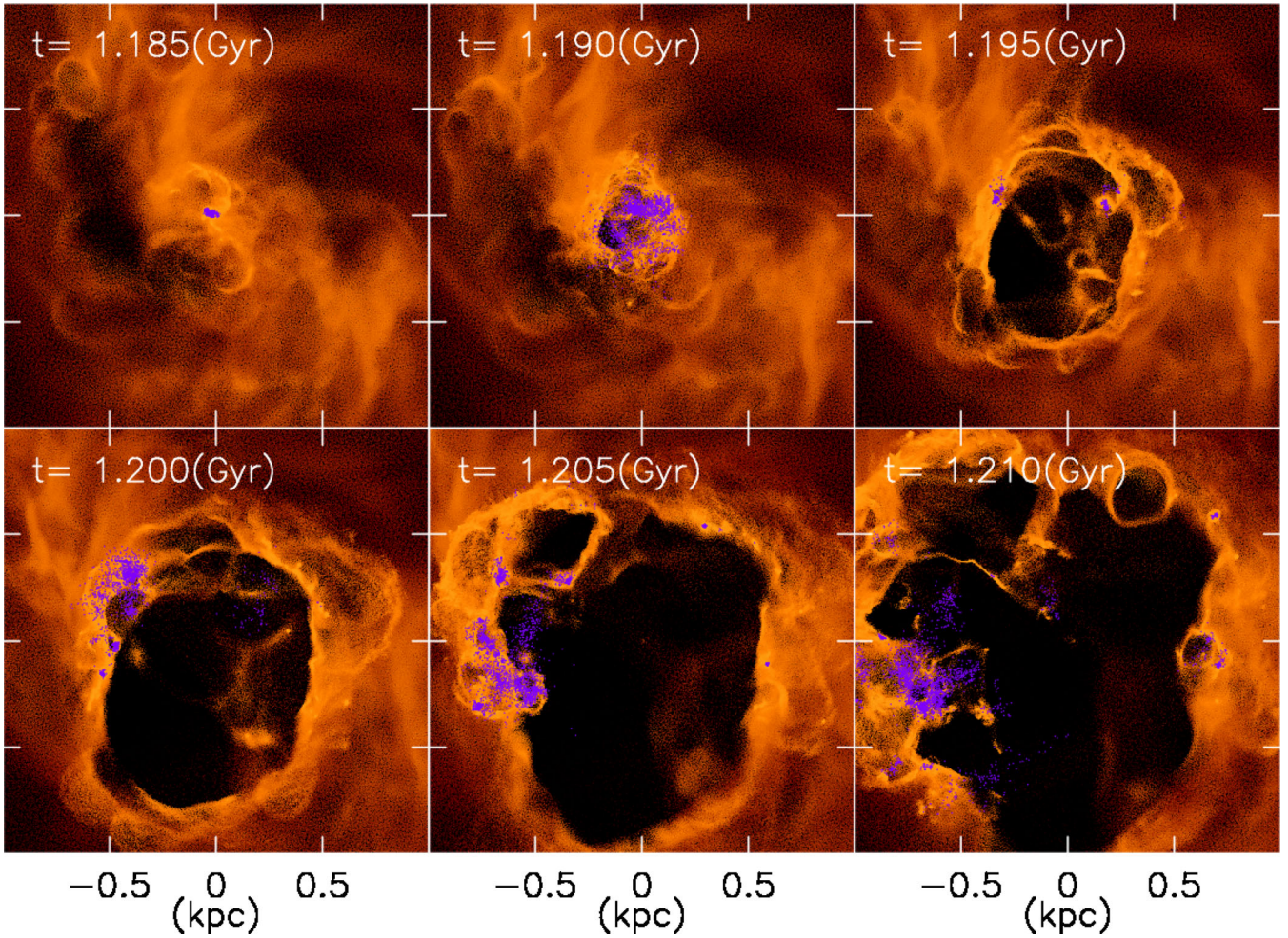


Figure 6. Close-up face-on view of the evolution of the gas distribution of Model FB. The blue dots indicate the star particles formed within the last 5 Myr.

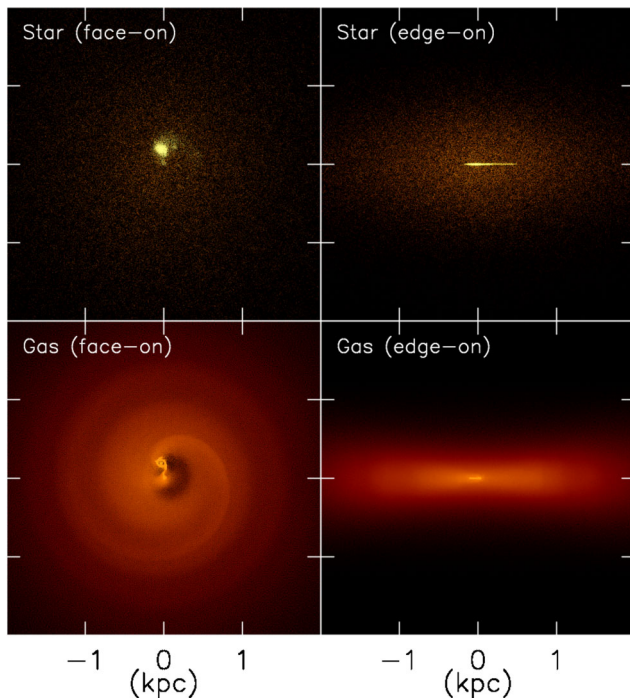


Figure 7. A snapshot of Model noFB at $t = 1.5$ Gyr.

stellar disc, mass accretion history and background radiation field. Also, exploring the critical mass is not the aim of this study.

Rather, our idealized simulations show that there can be small enough galaxies where spiral arms cannot be developed due to too shallow potentials and inefficient cooling. In such small galaxies, the bubble-induced star formation can make the star formation area bigger. In this case, the size of the galaxy could be determined where the density of the ISM becomes so small that the expanding bubbles no longer accumulate enough ISM to build up high-density shells. Edge-on views in Fig. 5 show that this is true also for the perpendicular direction to the disc. The bubbles and star-forming regions also propagate perpendicular to the disc. This can explain a high scaleheight of dIrrs. Fig. 8 demonstrates this more quantitatively. Fig. 8 shows the radial and vertical stellar surface density profiles for Models FB and noFB at $t = 1.5$ Gyr, comparing with the initial surface density profiles. In Model noFB, the stellar mass increases only in the central region ($R < 400$ pc).⁵ On the other hand, although there is a small excess in the central region, Model FB shows the increase of the stellar surface density at a wide range

⁵ Radial surface density profile of Model noFB shows an offset between the centre of the dark matter halo and stellar density peak. This is also seen in Fig. 7. Note that the centre of Figs 4–8 is set to be the centre of the dark matter halo.

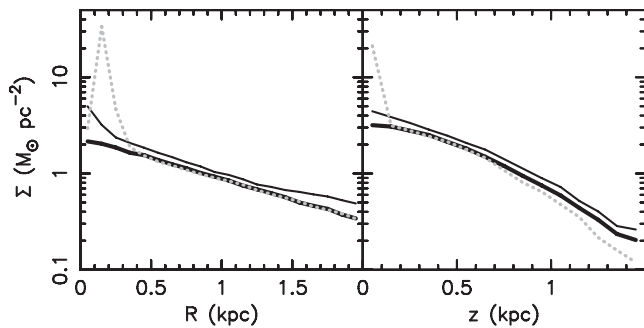


Figure 8. Radial (left) and vertical (right) stellar surface mass density profile for the initial disc (thick black solid) and Models FB (black solid) and noFB (grey dotted) at $t = 1.5$ Gyr. The vertical surface mass density was measured within the range of $0 < x < 0.5$ kpc.

of radii and vertical height, and the overall shape of both radial and vertical profiles at $t = 1.5$ Gyr is similar to the initial profile.

Fig. 5 also shows that there are some stars escaping from the disc region. These could be identified as halo stars, as discussed in the previous simulation studies (Stinson et al. 2009). It is also worth noting that because the ISM is continually disturbed by many generations of stellar feedback bubbles, the reaccretion of the gas is not circularly symmetric, and the star-forming region owing to the collisions with bubbles are not symmetric, e.g. a snapshot of $t = 1.205$ Gyr in Fig. 6. Such non-symmetric star-forming regions and bubbles are often observed in dIrrs (e.g. Kepley et al. 2007), which can be also explained by the bubble-induced star formation demonstrated by Model FB.

3.1 Metallicity

Fig. 9 shows the metallicity of the stars formed during the simulations. Model FB shows that the metallicity of the new born stars is almost constant and kept low. On the other hand, in Model noFB, the metallicity of the new born stars increases with their formation time. In this model, stars are forming only in the central region. The new born stars enrich the gas only in the central region. The metallicity of the gas in the central region quickly goes up. Therefore, the later generation of stars inevitably become metal rich. The metallicity reaches higher than the solar metallicity. The mean metallicity of the stars formed within the last 100 Myr is $[Z] = 0.023$, and this is unacceptably high. In Model FB, a similar amount of star formation took place. However, the metallicity of the new born stars is low. This is because the galaxy has a large reservoir of the metal-poor ISM, and the bubble-induced star formation enhances the mixing between the ISM and the metal-rich bubbles. Fig. 10 displays hydrogen number density, temperature, metallicity and velocity field of the gas at the disc plane of Model FB at $t = 1.195$ Gyr. As expected, the metallicity is very high within the bubble. However, the density within the bubble is too low and temperature is too high for star formation. As demonstrated above, the star formation can happen only within the high-density shells of the bubbles. Fig. 10 demonstrates that the cold high-density shells have metallicity as low as the surrounding ISM, which indicates that the ejected metals from feedback particles are well mixed with the ISM, when the gas density reaches the star formation threshold. In other words, the bubble-induced star formation guarantees the widely spread star formation and also keeps the metallicity of the star-forming region low. Note that the dispersion of the metallicity in Model FB is too small, and it is inconsistent with the variation of the estimated abun-

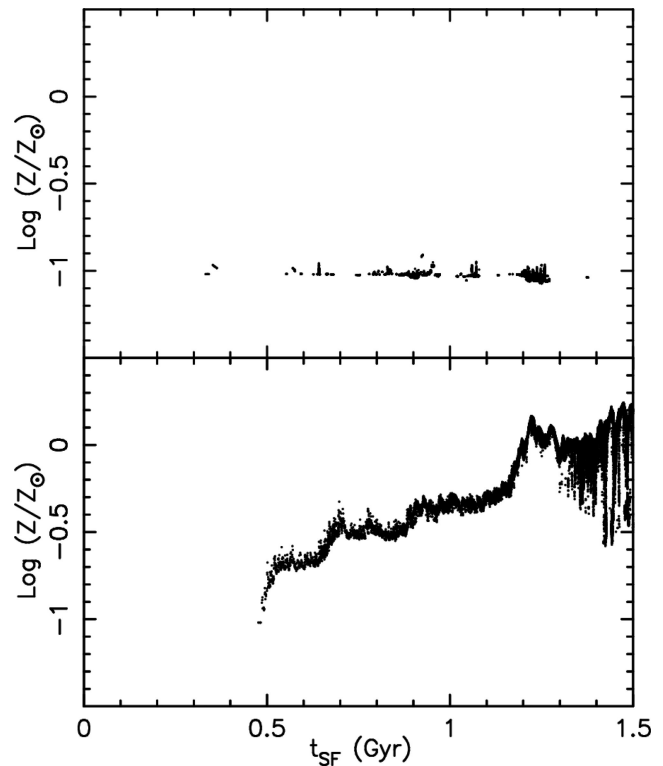


Figure 9. Metallicity of new born stars as a function of the formation time for Models FB (upper) and noFB (lower).

dances for the observed young stars in WLM which shows $[Z]$ from about -0.5 dex to -1 dex (Urbaneja et al. 2008). We therefore think that the metal diffusion in our simulations is likely to be over-estimated. We need to calibrate the metal diffusion model more. Comparisons between more observations in various dIrrs and the simulations like those used in this paper would be an effective way to improve the metal diffusion model. Calibrating the efficiency of metal diffusion via metallicity distribution function echoes the conclusions drawn by Pilkington et al. (2012) and Gibson et al. (2013).

3.2 Kinematics

It is interesting to see from the velocity field of Fig. 10 that some bubble shells are expanding faster than the rotation speed of the ISM, and some shells are moving against the rotational direction of the galactic disc. It can also be expected that if the bubbles are expanding from stars that are more slowly rotating than the gas, they collide with the ISM more violently on the back side, i.e. the opposite side to the rotation direction, than on the front side. Therefore, if the bubble-induced star formation is the dominant mechanism of star formation in dIrrs, we expect that more young stars are rotating slower than the ISM. Because the rotation velocity of dIrrs is small and can be smaller than the expansion speed of some bubbles, we expect many counter-rotating stars.

Fig. 11 displays the rotation velocity of the stars formed in the simulation period, i.e. $t_{\text{SF}} = 0-1.5$ Gyr, as a function of radius for Model FB at $t = 1.5$ Gyr. The figure shows that there are a significant number of counter-rotating stars, and the mean rotation speed is almost zero. Fig. 10 of Leaman et al. (2012) shows that in WLM especially within 1 kpc (assuming 1 arcmin = 0.25 kpc), the mean rotation velocity of stars is as low as 5 km s^{-1} . This is similar to the

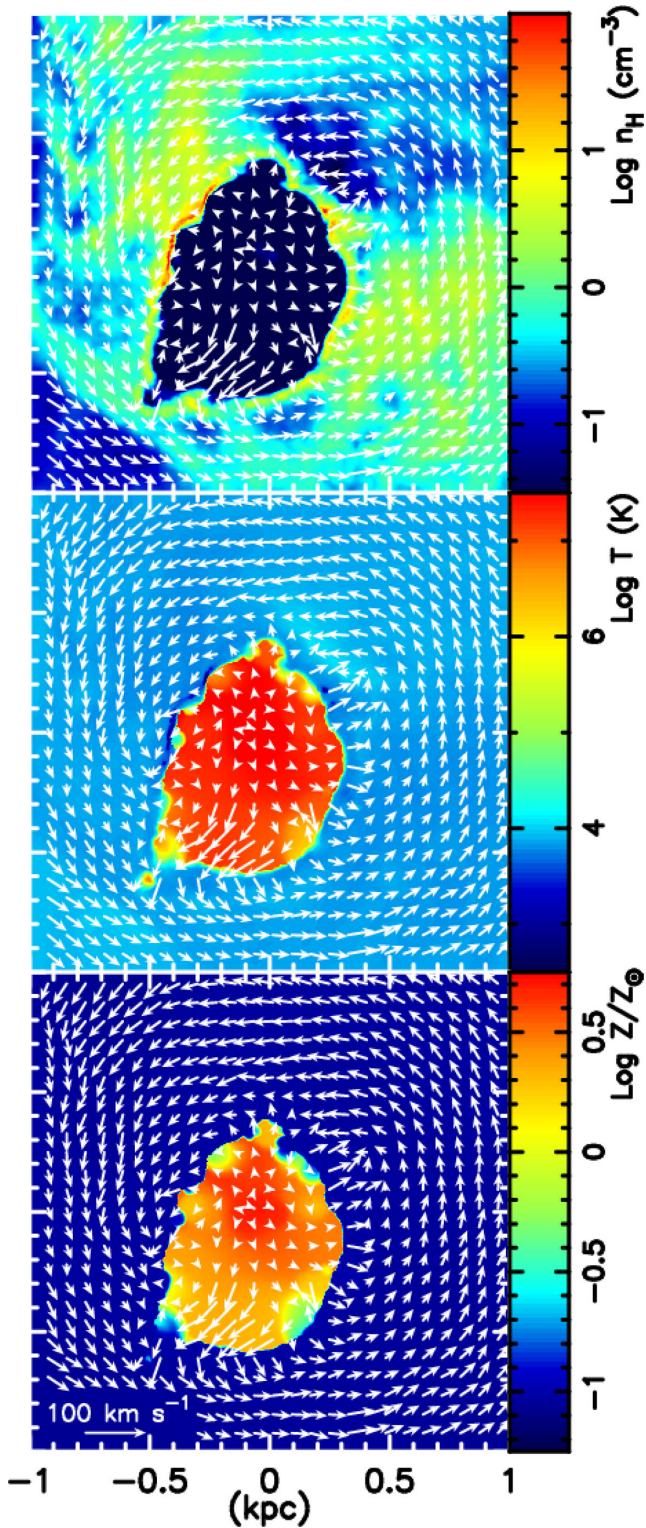


Figure 10. Hydrogen number density (top), temperature (middle) and metallicity (bottom) of the gas at the disc plane, $z = 0$, of Model FB at $t = 1.195$. The arrows (same in all the panels) indicate the gas velocity field.

maximum rotation in Model FB, $V_{\text{rot,max}} \sim 4 \text{ km s}^{-1}$. We note that our idealized simulations do not include the later gas accretion from the intergalactic medium, and our simulation likely underestimates the rotation of the ISM especially in the outer region. Feedback of

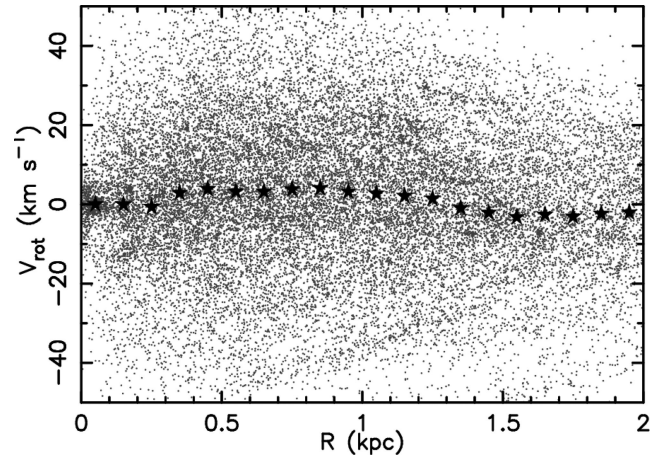


Figure 11. The rotation velocity as a function of the radius of the stars born (grey dots) during the 1.5 Gyr evolution for Model FB at $t = 1.5$ Gyr. The black stars indicate the mean rotation velocity at the different radii.

Model FB might be too high, too. Nevertheless, we still think from these results that the significant number of counter-rotating stars are an inevitable consequence of the bubble-induced star formation. It would be an interesting observational test to measure the mean rotation velocity and the fraction of the counter-rotating stars more accurately.

4 SUMMARY

We present numerical simulations of the evolution of a dIrr similar in size to WLM using the updated version of our original N -body/SPH chemodynamics code, `GCD+`. Our high-resolution simulations enable us to study how the strong feedback affects the ISM and star formation in small galaxies.

The simulation without stellar energy feedback has star formation only in the central region, where the gas density can become high enough for star formation. In this small system, the gravitational potential is shallow and radiative cooling is inefficient. As a result, the gas disc is stable to local instabilities except in the central region, and consequently, no structures such as spiral arms can develop. Therefore, the smooth gas accretion to the central region is the only way to reach a high enough gas density to form stars.

On the other hand, our strong feedback model demonstrates that once the bubbles are created by stellar feedback, the bubbles can collide with the ISM and/or the other bubbles, and create the dense filaments, where the gas density becomes high enough to form the next generation of stars. Such generations of stars can propagate outwards until the ISM density becomes too low for the bubbles to accumulate enough ISM to build up the dense shells. These successive bubbles induced by the generations of star formation can therefore produce the stars in the larger area compared to the model without the stellar energy feedback.

Our simulation with feedback also demonstrates that despite the large amount of metals produced by the new generation of stars, the metallicity of the star-forming region is kept low, because the metals produced are well mixed with the metal-poor ISM before they reach high enough density for star formation. We also find that the bubble-induced star formation leads to significantly lower rotation velocity of new born stars, compared to the gas. As a result, in a small system like dIrr, there will be many counter-rotating stars produced if the bubble-induced star formation is a dominant mechanism in dIrr.

We conclude that the bubble-induced star formation is one way to maintain a widely spread star formation, low metallicity, low stellar rotation velocity and high stellar velocity dispersion observed in dIrr. This is different from spiral-arm-induced star formation (Roberts 1969; Elmegreen 2011), where the star formation predominantly occurs in and around the spiral arms as seen in larger spiral galaxies both in observational studies (e.g. Rand & Kulkarni 1990; Foyle et al. 2011; Ferreras et al. 2012) and in numerical simulations (e.g. Wada & Koda 2004; Wada 2008; Dobbs & Pringle 2010; Wada, Baba & Saitoh 2011; Grand, Kawata & Cropper 2012). Still, the bubble-induced star formation can be important in large spiral galaxies, as seen in the superbubbles in the Milky Way (e.g. Oey et al. 2005), although the scale of the influence would be relatively smaller in the large galaxies, because of the higher density in the gas disc. Also, significant velocity dispersion of the H I gas is often observed in spiral galaxies (Dib, Bell & Burkert 2006; Tamburro et al. 2009), which can be maintained by the bubble-induced star formation as shown in our lower resolution simulations (Rahimi & Kawata 2012). Although it is computationally challenging, we are preparing for the simulations of larger spiral galaxies with similar physical resolution to this paper. We will explore the effect of bubble-induced star formation on larger spiral galaxies and compare with the case of small galaxies.

ACKNOWLEDGEMENTS

We thank an anonymous referee for their constructive comments and helpful suggestions which have improved the manuscript. BKG acknowledges the support of the UK's Science & Technology Facilities Council (STFC, ST/J001341/1). The calculations for this paper were performed on the UCL Legion, the Cray XT4 at Center for Computational Astrophysics (CfCA) of National Astronomical Observatory of Japan and the DiRAC Facilities (through the COSMOS consortium) jointly funded by STFC and the Large Facilities Capital Fund of BIS. We also acknowledge PRACE for awarding us access to resource Cartesius based in Netherlands at SURFsara.

REFERENCES

Barnes D. G., de Blok W. J. G., 2004, *MNRAS*, 351, 333
 Barnes D. J., Kawata D., Wu K., 2012, *MNRAS*, 420, 3195
 Bate M. R., Burkert A., 1997, *MNRAS*, 288, 1060
 Bekki K., Shigeyama T., Tsujimoto T., 2013, *MNRAS*, 428, L31
 Bianchi L., Efremova B., Hodge P., Massey P., Olsen K. A. G., 2012, *AJ*, 143, 74
 Booth C. M., Theuns T., Okamoto T., 2007, *MNRAS*, 376, 1588
 Brook C. B., Kawata D., Gibson B. K., Flynn C., 2004, *MNRAS*, 349, 52
 Carraro G., Chiosi C., Girardi L., Lia C., 2001, *MNRAS*, 327, 69
 Colucci J. E., Bernstein R. A., 2011, in Koleva M., Prugniel P., Vauglin I., eds, *EAS Publ. Ser. Vol. 48, Detailed Chemical Abundances of Globular Clusters in Local Group Dwarf Galaxies*. Cambridge Univ. Press, Cambridge, p. 275
 D'Onghia E., Vogelsberger M., Hernquist L., 2013, *ApJ*, 766, 34
 Dale J. E., Bonnell A., Clarke C. J., Bate M. R., 2005, *MNRAS*, 358, 291
 Dale J. E., Ercolano B., Bonnell I. A., 2013, *MNRAS*, 431, 1062
 Dalla Vecchia C., Schaye J., 2012, *MNRAS*, 426, 140
 Di Cintio A., Brook C. B., Maccio A. V., Stinson G. S., Knebe A., Dutton A. A., Wadsley J., 2013, *MNRAS*, 437, 415
 Dib S., Bell E., Burkert A., 2006, *ApJ*, 638, 797
 Dobbs C. L., Pringle J. E., 2010, *MNRAS*, 409, 396
 Dolphin A. E., 2000, *ApJ*, 531, 804
 Durier F., Dalla Vecchia C., 2012, *MNRAS*, 419, 465
 Efstathiou G., 1992, *MNRAS*, 256, 43P

Elmegreen B. G., 2011, in Charbonnel C., Montmerle T., eds, *EAS Publ. Ser. Vol. 51, Star Formation in Spiral Arms*. Cambridge Univ. Press, Cambridge, p. 19
 Elmegreen B. G., Rubio M., Hunter D. A., Verdugo C., Brinks E., Schruha A., 2013, *Nature*, 495, 487
 Fenner Y., Gibson B. K., Gallino R., Lugaro M., 2006, *ApJ*, 646, 184
 Ferland G. J., Korista K. T., Verner D. A., Ferguson J. W., Kingdon J. B., Verner E. M., 1998, *PASP*, 110, 761
 Ferreras I., Cropper M., Kawata D., Page M., Hoversten E. A., 2012, *MNRAS*, 424, 1636
 Foyle K., Rix H.-W., Dobbs C. L., Leroy A. K., Walter F., 2011, *ApJ*, 735, 101
 Gibson B. K., 1994, *MNRAS*, 271, L35
 Gibson B. K., 2007, in Vazdekis A., Peletier R., eds, *Proc. IAU Symp. 241, Stellar Populations as Building Blocks of Galaxies*. Cambridge Univ. Press, Cambridge, p. 161
 Gibson B. K., Pilkington K., Brook C. B., Stinson G. S., Bailin J., 2013, *A&A*, 554, A47
 Gingold R. A., Monaghan J. J., 1977, *MNRAS*, 181, 375
 Governato F. et al., 2010, *Nature*, 463, 203
 Grand R. J. J., Kawata D., Cropper M., 2012, *MNRAS*, 426, 167
 Greif T. H., Glover S. C. O., Bromm V., Klessen R. S., 2009, *MNRAS*, 392, 1381
 Haardt F., Madau P., 1996, *ApJ*, 461, 20
 Hodge P., Miller B. W., 1995, *ApJ*, 451, 176
 Hopkins P. F., Quataert E., Murray N., 2011, *MNRAS*, 417, 950
 Hopkins P. F., Quataert E., Murray N., 2012a, *MNRAS*, 421, 3488
 Hopkins P. F., Quataert E., Murray N., 2012b, *MNRAS*, 421, 3522
 Hopkins P. F., Keres D., Murray N., Hernquist L., Narayanan D., Hayward C. C., 2013, *MNRAS*, 433, 78
 Huchtmeier W. K., Seiradakis J. H., Materne J., 1981, *A&A*, 102, 134
 Hunter D. A., Elmegreen B. G., 2006, *ApJS*, 162, 49
 Hunter D. A., Elmegreen B. G., Ludka B. C., 2010, *AJ*, 139, 447
 Hunter D. A., Zahedy F., Bowsher E. C., Wilcots E. M., Kepley A. A., Gaal V., 2011, *AJ*, 142, 173
 Iwamoto K., Brachwitz F., Nomoto K., Kishimoto N., Umeda H., Hix W. R., Thielemann F., 1999, *ApJS*, 125, 439
 Jackson D. C., Skillman E. D., Cannon J. M., Côté S., 2004, *AJ*, 128, 1219
 Jackson D. C., Skillman E. D., Gehrz R. D., Polomski E., Woodward C. E., 2007, *ApJ*, 656, 818
 Kaufmann T., Wheeler C., Bullock J. S., 2007, *MNRAS*, 382, 1187
 Kawata D., Gibson B. K., 2003a, *MNRAS*, 340, 908
 Kawata D., Gibson B. K., 2003b, *MNRAS*, 346, 135
 Kawata D., Arimoto N., Cen R., Gibson B. K., 2006, *ApJ*, 641, 785
 Kawata D., Okamoto T., Gibson B. K., Barnes D. J., Cen R., 2013, *MNRAS*, 428, 1968
 Kay S. T., Pearce F. R., Frenk C. S., Jenkins A., 2002, *MNRAS*, 330, 113
 Kepley A. A., Wilcots E. M., Hunter D. A., Nordgren T., 2007, *AJ*, 133, 2242
 Kobayashi C., Tsujimoto T., Nomoto K., 2000, *ApJ*, 539, 26
 Leaman R. et al., 2012, *ApJ*, 750, 33
 Leaman R. et al., 2013, *ApJ*, 767, 131
 Lee H., Skillman E. D., Venn K. A., 2005, *ApJ*, 620, 223
 Lia C., Portinari L., Carraro G., 2002, *MNRAS*, 330, 821
 Lucy L. B., 1977, *AJ*, 82, 1013
 Mac Low M.-M., Ferrara A., 1999, *ApJ*, 513, 142
 Martínez-Serrano F. J., Serna A., Domínguez-Tenreiro R., Mollá M., 2008, *MNRAS*, 388, 39
 Mashchenko S., Couchman H. M. P., Wadsley J., 2006, *Nature*, 442, 539
 Mateo M. L., 1998, *ARA&A*, 36, 435
 Melotte P. J., 1926, *MNRAS*, 86, 636
 Merlin E., Buonomo U., Grassi T., Piovani L., Chiosi C., 2010, *A&A*, 513, A36
 Minniti D., Zijlstra A. A., 1997, *AJ*, 114, 147
 Mori M., Yoshii Y., Tsujimoto T., Nomoto K., 1997, *ApJ*, 478, L21
 Mori M., Yoshii Y., Nomoto K., 1999, *ApJ*, 511, 585
 Morris J., Monaghan J. J., 1997, *J. Comput. Phys.*, 136, 41
 Navarro J. F., White S. D. M., 1993, *MNRAS*, 265, 271

Navarro J. F., Eke V. R., Frenk C. S., 1996, *MNRAS*, 283, L72
 Navarro J. F., Frenk C. S., White S. D. M., 1997, *ApJ*, 490, 493
 Oey M. S., Massey P., 1994, *ApJ*, 425, 635
 Oey M. S., Watson A. M., Kern K., Walth G. L., 2005, *AJ*, 129, 393
 Pelupessy F. I., van der Werf P. P., Icke V., 2004, *A&A*, 422, 55
 Pilkington K. et al., 2011, *MNRAS*, 417, 2891
 Pilkington K. et al., 2012, *MNRAS*, 425, 969
 Pontzen A., Governato F., 2012, *MNRAS*, 421, 3464
 Price D. J., Monaghan J. J., 2007, *MNRAS*, 374, 1347
 Rahimi A., Kawata D., 2012, *MNRAS*, 422, 2609
 Rand R. J., Kulkarni S. R., 1990, *ApJ*, 349, L43
 Read J. I., Gilmore G., 2005, *MNRAS*, 356, 107
 Read J. I., Hayfield T., 2012, *MNRAS*, 422, 3037
 Rejkuba M., Minniti D., Gregg M. D., Zijlstra A. A., Alonso M. V., Goudfrooij P., 2000, *AJ*, 120, 801
 Revaz Y., Jablonka P., 2012, *A&A*, 538, A82
 Ricotti M., Gnedin N. Y., 2005, *ApJ*, 629, 259
 Roberts W. W., 1969, *ApJ*, 158, 123
 Robertson B. E., Kravtsov A. V., 2008, *ApJ*, 680, 1083
 Rodionov S. A., Athanassoula E., Sotnikova N. Y., 2009, *MNRAS*, 392, 904
 Rosswog S., Price D., 2007, *MNRAS*, 379, 915
 Saitoh T. R., Makino J., 2009, *ApJ*, 697, L99
 Saitoh T. R., Makino J., 2010, *PASJ*, 62, 301
 Saitoh T. R., Makino J., 2013, *ApJ*, 768, 44
 Saitoh T. R., Daisaka H., Kokubo E., Makino J., Okamoto T., Tomisaka K., Wada K., Yoshida N., 2008, *PASJ*, 60, 667
 Salpeter E. E., 1955, *ApJ*, 121, 161
 Sawala T., Guo Q., Scannapieco C., Jenkins A., White S., 2011, *MNRAS*, 413, 659
 Schaye J., 2004, *ApJ*, 609, 667
 Schaye J., Dalla Vecchia C., 2008, *MNRAS*, 383, 1210
 Schroyen J., De Rijcke S., Koleva M., Cloet-Osselaer A., Vandenbroucke B., 2013, *MNRAS*, 434, 888
 Shull J. M., 1980, *ApJ*, 238, 860
 Silich S., Lozinskaya T., Moiseev A., Podorvanuk N., Rosado M., Borissowa J., Valdez-Gutierrez M., 2006, *A&A*, 448, 123
 Simpson C. M., Bryan G. L., Johnston K. V., Smith B. D., Mac Low M.-M., Sharma S., Tumlinson J., 2013, *MNRAS*, 432, 1989
 Skillman E. D., Terlevich R., Melnick J., 1989, *MNRAS*, 240, 563
 Springel V., Hernquist L., 2002, *MNRAS*, 333, 649
 Springel V., Hernquist L., 2003, *MNRAS*, 339, 289
 Springel V., Di Matteo T., Hernquist L., 2005, *MNRAS*, 361, 776
 Stilp A. M., Dalcanton J. J., Warren S. R., Skillman E., Ott J., Koribalski B., 2013, *ApJ*, 765, 136
 Stinson G., Seth A., Katz N., Wadsley J., Governato F., Quinn T., 2006, *MNRAS*, 373, 1074
 Stinson G. S., Dalcanton J. J., Quinn T., Kaufmann T., Wadsley J., 2007, *ApJ*, 667, 170
 Stinson G. S., Dalcanton J. J., Quinn T., Gogarten S. M., Kaufmann T., Wadsley J., 2009, *MNRAS*, 395, 1455
 Tamburro D., Rix H.-W., Leroy A. K., Mac Low M.-M., Walter F., Kennicutt R. C., Brinks E., de Blok W. J. G., 2009, *AJ*, 137, 4424
 Teyssier R., Pontzen A., Dubois Y., Read J. I., 2013, *MNRAS*, 429, 3068
 Thacker R. J., Couchman H. M. P., 2000, *ApJ*, 545, 728
 Thornton K., Gaudlitz M., Janka H.-T., Steinmetz M., 1998, *ApJ*, 500, 95
 Tortora C., Napolitano N. R., Cardone V. F., Capaccioli M., Jetzer P., Molinaro R., 2010, *MNRAS*, 407, 144
 Urbaneja M. A., Kudritzki R.-P., Bresolin F., Przybilla N., Gieren W., Pietrzyński G., 2008, *ApJ*, 684, 118
 Vader J. P., Vigroux L., Lachize-Rey M., Souvion J., 1988, *A&A*, 203, 217
 van den Hoek L. B., Groenewegen M. A. T., 1997, *A&AS*, 123, 305
 Venn K. A., Tolstoy E., Kaufer A., Skillman E. D., Clarkson S. M., Smart S. J., Lennon D. J., Kudritzki R. P., 2003, *AJ*, 126, 1326
 Wada K., 2008, *ApJ*, 675, 188
 Wada K., Koda J., 2004, *MNRAS*, 349, 270
 Wada K., Baba J., Saitoh T. R., 2011, *ApJ*, 735, 1
 Weaver R., McCray R., Castor J., Shapiro P., Moore R., 1977, *ApJ*, 218, 377

Wolf M., 1909, *Astron. Nachr.*, 183, 187
 Woosley S. E., Weaver T. A., 1995, *ApJS*, 101, 181

APPENDIX A: LOWER RESOLUTION MODEL

We present the results of three complementary lower resolution models, Models LRFB1, LRFB2 and LRLH. All models use 10 times fewer particles, i.e. the mass of star and gas particles is $1000 M_{\odot}$. We employ the minimum softening length of 34 pc for the baryon particles. Note that our stellar feedback scheme is not designed to be resolution independent. Instead, we adopt a simple scheme, which has less parameters, but is sensitive to the resolution. We can still calibrate the feedback parameters at a fixed physical resolution. The aims of these complementary models are to demonstrate that our qualitative conclusion is robust against the numerical resolution, the choice of star formation parameters, such as $n_{\text{H,th}}$ and C_* (see Section 2.1), and if or not a live dark matter halo is adopted.

Model LRFB1 is similar to Model FB and uses $n_{\text{H,th}} = 1000 \text{ cm}^{-3}$ and $C_* = 1.0$. On the other hand, Model LRFB2 employs $n_{\text{H,th}} = 10 \text{ cm}^{-3}$ and $C_* = 0.02$. Fig. A1 shows the SFR history for Models LRFB1 and LRFB2. Model LRLH employs the same C_* and $n_{\text{H,th}}$ as Model LRFB1. However, Model LRLH adopts a live dark matter halo, which is described by $10^4 M_{\odot}$ collisionless particle with the softening length of 73 pc. To reduce the total number of dark matter particles, we adopted a truncated NFW profile (Rodionov, Athanassoula & Sotnikova 2009),

$$\rho_{\text{dm}} = \frac{3H_0^2}{8\pi G} \frac{\Omega_0 - \Omega_b}{\Omega_0} \frac{\rho_c}{cx(1+cx)^2} \exp(-x^2 r_{200}^2 / r_t^2), \quad (\text{A1})$$

where r_t is the truncation radius, and we set $r_t = 13.9 \text{ kpc}$. We apply $c = 20$ for the initial condition of Model LRLH which is significantly higher than $c = 12$ used for the fixed halo case. However, we find that the dark matter density profile becomes shallower in the live halo case (Fig. A2), which leads to a similar profile to the NFW profile with $c = 12$.

Comparing Model LRFB1 with Model FB (Fig. 3), although Model LRFB1 shows stochastic star formation due to the bubble-induced star formation, it starts much later ($t \sim 3.5 \text{ Gyr}$) than Model FB. This is because in the lower resolution model it takes a longer time to accumulate enough gas into the central region to cause the bubble-induced star formation and outward propagation of star-forming region. In addition, at the earlier time, the central region is fragile against stellar feedback, because less gas accretes into the central region, even when the gas density reaches high enough density for star formation at the very centre. This causes the three bursts ($t \sim 1.2, 2.1$ and 3.0 Gyr) with a longer quiescent period in between.

Because of the lower threshold density for star formation, Model LRFB2 has the first burst at an earlier epoch ($t \sim 0.6 \text{ Gyr}$). However, at this time, the central region does not have enough gas accumulated to cause the bubble-induced star formation and is fragile against stellar feedback. This delays the accumulation of gas in the central region and the onset of the bubble-induced star formation. The SFR history around $t \sim 4\text{--}5.5 \text{ Gyr}$ for Model LRFB2 looks smoother and less bursty than that for Model LRFB1. However, we observe the bubble-induced star formation, i.e. the star formation happens in the shells of the bubbles and propagates outwards.

Because of the higher concentration, which helps accumulating enough gas into the central region, Model LRLH starts the bubble-induced star formation earlier ($t \sim 2.6 \text{ Gyr}$) than the other models. It is surprising to see that the first burst of star formation is later ($t \sim 2.0 \text{ Gyr}$) in Model LRLH than Model LRFB1 ($t \sim 1.2 \text{ Gyr}$).

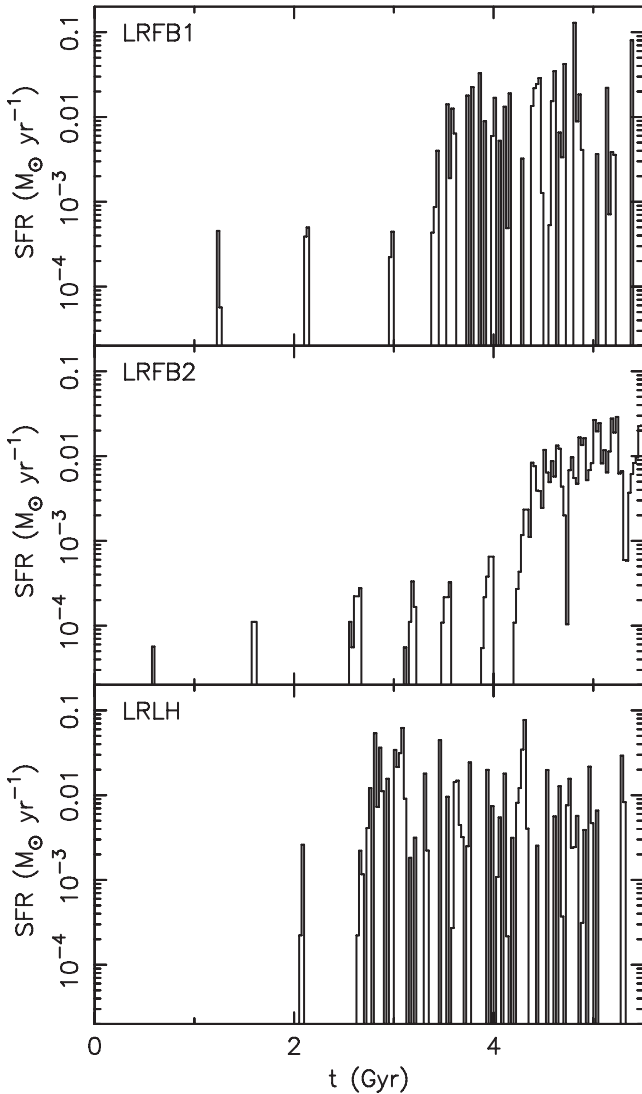


Figure A1. History of SFR of Models LRFB1 (upper), LRFB2 (middle) and LRLH (bottom).

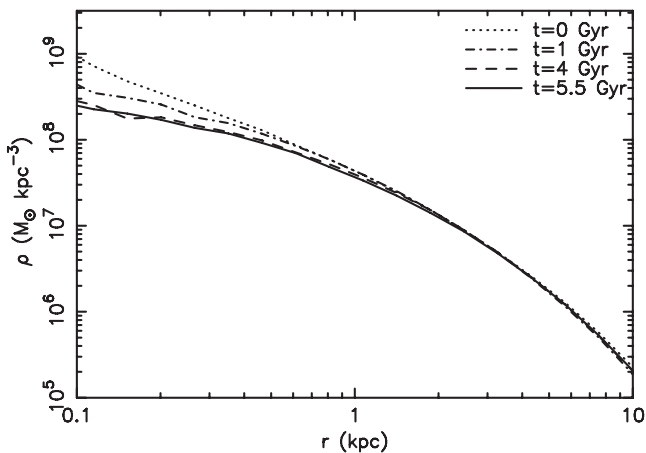


Figure A2. Radial dark matter mass density profile for Model LRLH at $t = 0$ Gyr (dotted), $t = 1$ Gyr (dot-dashed), $t = 4$ Gyr (dashed) and $t = 5.5$ Gyr (solid).

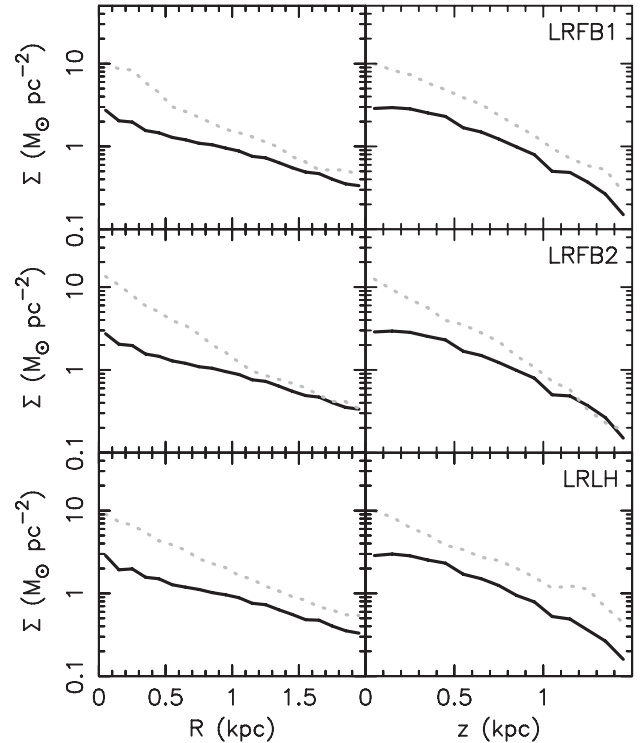


Figure A3. Radial (left) and vertical (right) stellar surface mass density profile for the initial disc (thick black solid) and the disc at $t = 5.5$ Gyr (grey dotted) for Models LRFB1 (upper), LRFB2 (middle) and LRLH (bottom). The vertical surface mass density was measured within the range of $0 < x < 0.5$ kpc.

This may be because the central density of the dark matter halo is limited at the scale of the resolution in the live dark matter halo, while the fixed dark matter halo follows the NFW profile without any limit.

The mean SFR for the last 1 Gyr ($t = 4.5$ – 5.5 Gyr) is $9.5 \times 10^{-3} M_{\odot} \text{ yr}^{-1}$ for Model LRFB1 and $1.1 \times 10^{-2} M_{\odot} \text{ yr}^{-1}$ for Model LRFB2. These SFR are slightly higher than that for Model FB. As we mentioned above, our feedback scheme is resolution dependent, and it is not surprising to see the difference between models with different resolutions. Models LRFB1 and LRFB2 show similar mean SFR. This demonstrates that both $n_{\text{H,th}}$ and C_* affect the resultant SFR, and applying high $n_{\text{H,th}}$ and C_* has a similar effect to using low $n_{\text{H,th}}$ and C_* . The mean SFR for the last 1 Gyr for Model LRLH is $3.6 \times 10^{-3} M_{\odot} \text{ yr}^{-1}$, which is smaller but similar to that for Model LRFB1.

Fig. A3 shows the radial and vertical surface mass density profile at $t = 0$ and 5.5 Gyr for Models LRFB1, LRFB2 and LRLH. Similar to Model FB in Fig. 8, all the models show the increase in the stellar surface density at a wide range of radii and vertical height. Model LRFB2 shows more increase in the inner region, which indicates more star formation in the inner region.

Fig. A4 shows the metallicity of stars formed in the last 2 Gyr of the evolution for Models LRFB1, LRFB2 and LRLH. Similar to Model FB in Fig. 9, the metallicity of new born stars is kept low, because of the efficient mixing between the metal-rich bubbles and the metal-poor ISM. Because of the high SFR, Model LRFB2 shows higher metallicity. Also, the low density threshold of star formation in Model LRFB2 causes more scatter in the metallicity, because the stars can form from lower density gas where the metallicity is more inhomogeneous (Fig. 10). As discussed in Section 3.1, our

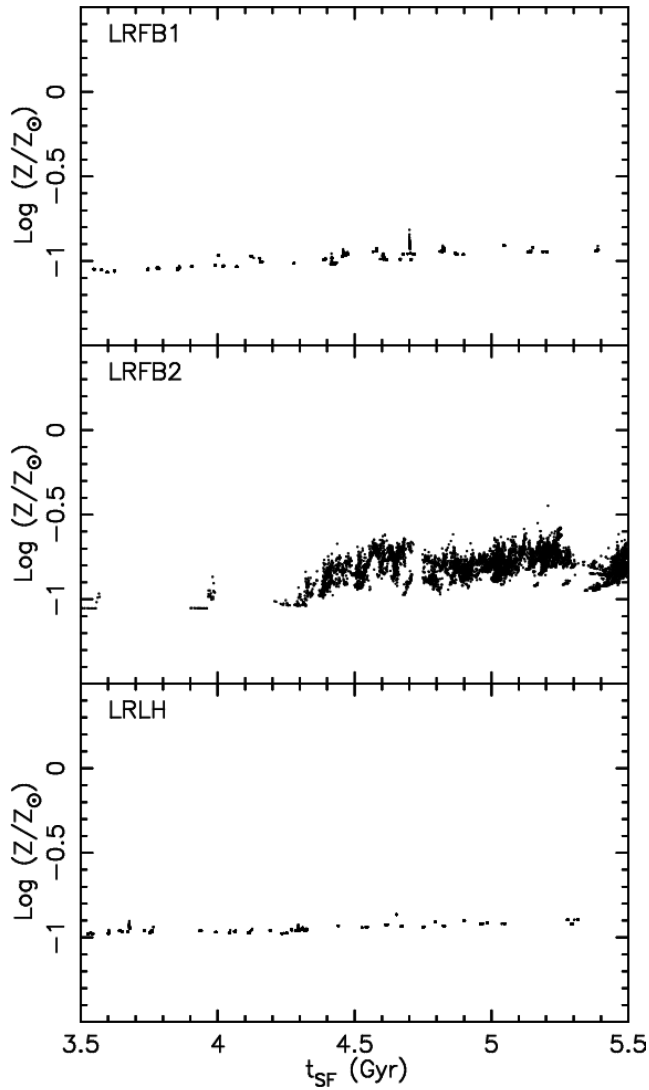


Figure A4. Metallicity of new born stars as a function of the formation time for Models LRFB1 (upper), LRFB2 (middle) and LRLH (bottom). There appear to be a fewer particles in Models LRFB1 and LRLH, because there are many star particles with almost same metallicity and formation time.

metal diffusion model needs to be calibrated more, and it is not independent from the star formation parameters.

Although there are several (expected) differences between the high- and low-resolution models, the overall results from the lower resolution simulations are qualitatively consistent with the higher resolution models. This reassures our conclusion about the bubble-induced star formation: the level of star formation and metallicity is kept low, while stars form in a widely spread area.

This paper has been typeset from a $\text{\TeX}/\text{\LaTeX}$ file prepared by the author.